NeuroImage 209 (2020) 116525

Contents lists available at ScienceDirect

NeuroImage

journal homepage: www.elsevier.com/locate/neuroimage

In vivo imaging of deep neural activity from the cortical surface during hippocampal epileptiform events in the rat brain using electrical impedance tomography

Sana Hannan [a,*], Mayo Faulkner [b], Kirill Aristovich [a], James Avery [c], Matthew C. Walker [d], David S. Holder [a]

[a] Department of Medical Physics and Biomedical Engineering, University College London, UK
[b] Wolfson Institute for Biomedical Research, University College London, UK
[c] Department of Surgery and Cancer, Imperial College London, UK
[d] UCL Queen Square Institute of Neurology, University College London, UK

ARTICLE INFO

Keywords:
EIT
Hippocampus
Cerebral cortex
Imaging
Tissue impedance
Epilepsy
Ictal spikes
Rat

ABSTRACT

Electrical impedance tomography (EIT) is a medical imaging technique which reconstructs images of the internal impedance changes within an object using non-penetrating surface electrodes. To date, EIT has been used to image fast neural impedance changes during somatosensory evoked potentials and epileptiform discharges through the rat cerebral cortex with a resolution of 2 ms and <300 μm. However, imaging of neural activity in subcortical structures has never been achieved with this technique. Here, we evaluated the feasibility of using EIT to image epileptiform activity in the rat hippocampus using non-penetrating electrodes implanted on the cortical surface. Hippocampal epileptiform events, comprising repetitive 30–50 Hz ictal spikes, were induced by electrically stimulating the perforant path of rats anaesthetised with fentanyl-isoflurane. For each of ≥30 seizures, impedance measurements were obtained by applying 100 μA current at 1.4 kHz through an independent pair of electrodes on a 54-electrode planar epicortical array and recording boundary voltages on all remaining electrodes. EIT images of averaged ictal spikes were reconstructed using impedance recordings from all seizures in each animal. These revealed a focus of neural activity localised to the dentate gyrus which was spatially and temporally aligned to local field potential (LFP) recordings and could be reconstructed reproducibly in all animals with a localisation accuracy of ≤400 μm ($p < 0.03125$, $N = 5$). These findings represent the first experimental evidence of the ability of EIT to image neural activity in subcortical structures from the surface of the cortex with high spatiotemporal resolution and suggest that this method may be used for improving understanding of functional connectivity between cortico-hippocampal networks in both physiological and pathophysiological states.

1. Introduction

1.1. Background

Despite the continuous development of novel anticonvulsants, over 30% of individuals with epilepsy remain resistant to pharmacotherapy and a proportion of these may benefit from neurosurgical resection of epileptogenic tissue (Kwan et al., 2011; Nair, 2016). Temporal lobe epilepsy (TLE) accounts for the majority (60–70%) of human focal epilepsies and represents almost two-thirds of cases of refractory epilepsy managed surgically (Berg et al., 2010; Blair, 2012). Mesial TLE is the most common form of TLE and is frequently characterised by the presence of its typical pathophysiological substrate, hippocampal sclerosis (Engel, 2001; Blair, 2012). This comprises severe neuronal cell loss and gliosis in the hippocampus which lead to alterations to local and widespread neuronal networks and is often the result of complex interactions between genetic and environmental factors (Berkovic et al., 1991; Walker, 2015). Such alterations may subsequently predispose these networks to become hyperexcitable, leading to seizure generation. Conversely, hippocampal sclerosis may itself be caused by prolonged seizures (Theodore et al., 1999). Mesial TLE with hippocampal sclerosis is one of the most refractory forms of epilepsy and individuals with this condition are commonly treated by surgical resection of epileptogenic lesions, localised using high-resolution MRI and video-EEG recordings

* Corresponding author.
E-mail address: sana.hannan@ucl.ac.uk (S. Hannan).

https://doi.org/10.1016/j.neuroimage.2020.116525
Received 9 October 2019; Received in revised form 12 December 2019; Accepted 6 January 2020
Available online 8 January 2020

from subdural grid electrodes or depth electrodes (Diehl and Lüders, 2000; Engel, 2001). However, seizure relapse ≥1 year post-surgery, following an initial seizure-free period, occurs significantly more in patients with mesial TLE compared to other epilepsy syndromes (Spencer, 1996; Hennessy et al., 2000; Spencer et al., 2003). This late recurrence of seizures may indicate inaccuracies in the presurgical localisation of the epileptogenic zone in addition to an incomplete understanding of the complex interplay between the structural and functional abnormalities underlying this condition.

Electrical impedance tomography (EIT) is a medical imaging modality which reconstructs images of the internal electrical impedance of an object from multiple transfer impedance measurements made with non-penetrating surface electrodes (Holder, 2005). Each individual impedance measurement is obtained by injecting current through a single electrode pair and recording the resulting boundary voltages from all remaining electrodes. EIT can be used to image impedance changes associated with neuronal depolarisation; as neurons are activated, the opening of voltage- and ligand-gated ion channels in their cell membranes enables current to pass into the intracellular space, which manifests as voltage changes on the recording electrodes (Klivington and Galambos, 1967; Oh et al., 2011). To date, this technique has been used in the anaesthetised rat to produce impedance images of neural activity in the cerebral cortex during physiological evoked activity (Aristovich et al., 2016) and epileptiform discharges (Hannan et al., 2018a) with a spatiotemporal resolution of 2 ms and ≤300 μm, using an epicortical electrode array.

Due to its ability to image neuronal depolarisation at a high spatiotemporal resolution throughout large volumes of cerebral tissue, EIT holds potential for use as an adjunct imaging modality during presurgical evaluation of patients with mesial TLE to improve localisation accuracy and thus post-surgical outcome, as well as a neuroimaging tool for use *in vivo* to aid understanding of hippocampal epileptogenic networks. However, fast neural impedance changes occurring in subcortical brain regions such as the hippocampus have never previously been imaged from the cortical surface. An *in silico* modelling study conducted by Aristovich et al. first suggested that imaging epileptiform activity in the hippocampus of the rat, simulated as a spherical perturbation with a 10% conductivity change in the CA1 field, with EIT using epicortical measurements is feasible (Aristovich et al., 2014). Their findings were in broad agreement with recent simulations which have characterised the sensitivity of EIT for detecting deep somatosensory evoked activity, modelled as a spherical perturbation with a conductivity change of 0.4%, using 57-electrode arrays placed on the rat cortical surface (Faulkner et al., 2018a). This study revealed that EIT has a depth sensitivity of ~2.5 mm to such physiological activity, which encompasses the depth of the cortex and extends to superficial regions of the hippocampus (Faulkner et al., 2018a). However, because epileptiform discharges are caused by the abnormal hypersynchronous activity of specific neuronal groups, they give rise to a larger impedance change than evoked potentials at a given carrier frequency of injected current (Faulkner et al., 2018b; Hannan et al., 2018b). This suggests that EIT may be capable of imaging epileptiform activity occurring deeper than 2.5 mm from the cortical surface.

The first step in understanding the therapeutic and research potential of EIT for mesial TLE is to determine whether the penetration depth of EIT with epicortical electrodes does indeed enable imaging of epileptiform activity originating in the hippocampus, as suggested by simulations (Aristovich et al., 2014; Faulkner et al., 2018a). For this purpose, use of a rodent model of epilepsy that generates hippocampal ictal discharges from a known focus is desirable. The hippocampal epileptic afterdischarges (ADs) model fulfils this requirement. It involves electrical stimulation of the perforant path, which projects onto the dentate granule cells and into the hippocampus proper, and results in the immediate induction of an epileptiform event in the hippocampus. The induced ictal events comprise repeatable series of rhythmic high-amplitude population spikes, <8 ms in duration, which represent the simultaneous generation of action potentials from a given population of dentate granule cells as a result of stimulation (Andersen et al., 1971; Bragin et al., 1997; Shepherd, 2004). This model thus produces an ictal focus localised to microcircuits within the dentate gyrus and hippocampus proper; as such, it can be used to assess whether it is possible to image hippocampal epileptiform events with EIT and subsequently determine the spatial accuracy of any imaged activity.

1.2. Purpose

The purpose of this work was to evaluate the feasibility of imaging ictal discharges localised to the hippocampus with EIT, using non-penetrating electrodes implanted on the cortical surface of the anaesthetised rat, and to evaluate the clinical and research potential of the proposed method. Specific questions to be answered were:

(i) Can EIT be used to produce biophysically plausible images of fast neural impedance changes during hippocampal ictal discharges from the surface of the cerebral cortex?
(ii) If so, what are the spatiotemporal features of the reconstructed activity and how do these compare to current understanding of the mechanisms of these discharges?

1.3. Experimental design

EIT was performed on one hemisphere of the brain of anaesthetised rats using a planar epicortical electrode array which contained 54 electrodes and two rectangular apertures at the appropriate locations to enable implantation of two depth electrodes: (a) a stimulating depth electrode for inducing ictal discharges in the hippocampus, and (b) a recording depth electrode to validate the presence of the hippocampal ictal discharges through LFP recordings. The hippocampal epileptic ADs model, which involves electrical stimulation of the angular bundle of the perforant path, was used to elicit ictal events in the hippocampus (**Supplementary Information 1.1**); these comprised a train of repetitive granule cell population spikes and will henceforth be termed 'seizures'. The main advantages of this model include its ability to induce frequent reproducible seizures with a known ictal focus on demand, which typically exhibit less electrographic variability than the spontaneous ictal events generated by chemical models of epilepsy, thus enabling complete control of the protocol for obtaining EIT measurements in this proof of concept study (Bragin et al., 1997; Walker et al., 1999; Colangeli et al., 2017).

An EIT measurement was obtained using an independent current-injecting electrode pair on the epicortical array during each of ≥30 electrically induced seizures. The decision to use an EIT protocol comprising 30 current-injecting electrode pairs was based on previous *in vivo* fast neural EIT studies, in which physiological evoked or epileptiform activity in the rat cortex were successfully imaged using this approach (Aristovich et al., 2016; Hannan et al., 2018a). Due to its low magnitude, the fast neural impedance responses to ictal discharges were averaged within seizures to achieve an adequate signal-to-noise ratio (SNR) for imaging, another approach utilised previously (Aristovich et al., 2016; Hannan et al., 2018a). However, the SNR of the impedance change during hippocampal ictal discharges as measured from the cortical surface was still expected to be considerably lower than that of the cortical activity imaged in these previous studies. Two EIT recording parameters, the carrier frequency and amplitude of the injected current, were therefore altered from what has been used previously to provide the best chance of imaging below the cerebral cortex. For obtaining EIT measurements, current was injected at 100 μA, which corresponds to a current density of 354 Am^{-2} when applied through the standard epicortical electrodes, 0.6 mm in diameter, used in *in vivo* fast neural EIT studies. This amplitude of EIT current was chosen as it is the highest current level that, when applied continuously to the rat cerebral cortex, does not affect the amplitude or latency of neural activity during

somatosensory evoked potentials (Oh et al., 2011) or cause any structural damage to the cortical tissue (Hannan et al., 2019). Use of this higher current amplitude was expected to increase current density, and thus sensitivity to impedance changes, in the hippocampus compared to previous fast neural EIT studies (Aristovich et al., 2016; Hannan et al., 2018a). Additionally, the carrier frequency of injected current was 1355 Hz, the optimal frequency for imaging impedance changes during epileptiform activity (Hannan et al., 2018b), to maximise the SNR of the measured impedance response.

2. Materials and methods

2.1. Animal preparation

All animal handling and experimental investigations undertaken in this study were ethically approved by the UK Home Office and performed in accordance with its regulations, as outlined in the Animals (Scientific Procedures) Act 1986. Five adult female Sprague-Dawley rats (405–460 g) were used for recordings. Anaesthesia was induced with 4% isoflurane in 2 L min^{-1} O_2 and an endotracheal intubation was performed to enable mechanical control of ventilation with 1.5–3% isoflurane in a 30/70 mixture of oxygen/air using an SAV03 ventilator (Vetronic Services Ltd, Abbotskerswell, UK). Cannulation of the right femoral vessels was undertaken to allow for monitoring of intra-arterial blood pressure and intravenous access. Exhaled gases, respiratory rate, tidal volume, heart rate, invasive arterial blood pressure and SpO_2 were monitored regularly using an anaesthetic monitor (Lightning; Vetronic Services Ltd., Abbotskerswell, UK) and core body temperature was maintained at 36.5 ± 0.5 °C using a homeothermic heating unit (Harvard Apparatus, Edenbridge, UK). The rat was then mounted in a stereotactic frame (Narishige International Ltd., London, UK) in the prone position using blunt-tipped interaural and incisor bars to restrain the head in a horizontal plane, the skull was exposed by incising the scalp and displacing the skin of the head. The mediolateral (ML) and dorsoventral (DV) coordinates of two anatomical landmarks on the skull, bregma and lambda, were determined using a needle attached to a micromanipulator (SM-15; Narishige International Ltd., London, UK) on an arm of the stereotactic frame. The position of the head was then adjusted until the ML and DV coordinates of bregma and lambda were both within 100 μm of each other; this ensured that the skull was aligned within the frame in the ML and DV axes. As such, a consistently high degree of accuracy in stereotactically localising the relevant intracranial targets, namely the angular bundle and hippocampal dentate gyrus, could be achieved across animals.

The insertion of the temporal muscle was cauterised using a bipolar coagulation unit (Codman Malis CMC-II; Codman, Raynham, MA) and incised with a scalpel. The cerebral cortex of the left hemisphere was then exposed through a craniotomy using a veterinary bone drill (Ideal Micro-Drill; Harvard Apparatus, Edenbridge, UK). The paramedial edge of the craniotomy extended from 1 mm anterior to lambda to 5 mm posterior to bregma, with the lateral boundary at the junction of the zygomatic arch and the temporal bone, forming a trapezoidal opening. The dura was incised and the exposed cortex frequently irrigated with 0.9% sterile saline at 37 °C until electrode implantation. All procedures were performed on a vibration isolated table (Thorlabs Inc., Newton, NJ, USA).

2.2. Electrode implantation

A planar custom-designed 54-contact epicortical electrode array, fabricated from stainless steel foil and silicone rubber, was then placed on the exposed cortical surface. The array was trapezoidal in shape and measured 15 × 9 mm at its furthest edges, providing coverage of ~90% of the neocortex of one cerebral hemisphere, and contained two rectangular apertures (**Supplementary Information 1.2**). The array was placed such that these apertures were centred over the respective anteroposterior (AP) and ML coordinates for implanting the stimulating and recording depth electrodes. The 54 epicortical electrodes, each 0.6 mm in diameter, were coated with PEDOT:pTS to reduce contact impedance across the electrode-electrolyte interface to ≤1 kΩ. The coordinates of the centres of at least four electrodes, each near a corner of the array, were determined with respect to bregma using a needle attached to a micromanipulator (SM-15; Narishige International Ltd., London, UK); these coordinates were used to ensure accuracy in modelling the positions of the epicortical electrodes on the mesh used for image reconstruction. This experiment-to-model coregistration process was further aided by taking photographs of the implanted epicortical array, in which the bregma and lambda reference points and sagittal suture were visible, from multiple angles.

The two depth electrodes were stereotactically positioned to be orthogonal to the exposed cortical surface at their respective coordinates, using micromanipulators, and gradually advanced ventrally through the apertures in the epicortical array to reach their target intracranial structures. The stimulating electrode comprised two twisted polydimide-insulated stainless steel wires (bare wire diameter: 125 μm; outer diameter: 203 μm) with 0.5 mm vertical tip separation (MS303/3-A/SPC; Plastics One Inc., Roanoke, VA, USA) and was implanted into left angular bundle to stimulate the medial perforant path afferents to the hippocampus (AP = −8.1, ML = 4.4, DV = 3.5 mm; AP and ML given with respect to bregma and DV given from cortical surface). The recording depth electrode comprised a 16-channel linear silicon neural probe (A1x16-10mm-100–703; NeuroNexus Technologies Inc., Ann Arbor, MI, USA). The 16 iridium electrode contacts, each 30 μm in diameter, had a centre-to-centre spacing of 100 μm and spanned a total length of 1.5 mm. The centre of the probe was directed to the granule cell layer of the dentate gyrus (AP = −4.0, ML = 2.5, DV = 2.8 mm) for recording LFPs to validate the presence of hippocampal epileptiform discharges following stimulation. Following implantation of both depth electrodes, anaesthesia was maintained with continuously-infused intravenous fentanyl at 20 μg/kg/h and ~0.5% isoflurane.

Confirmatory LFP recordings were made to ensure the correct placement of stimulating and recording depth electrodes. Evoked activity comprising a granule cell population spike superimposed on a field excitatory postsynaptic potential (fEPSP) was induced in the dentate gyrus by delivering 1 mA monopolar square-wave pulses, 150 μs in duration, to the stimulating electrode at a frequency of 0.5 Hz using a Neurolog current stimulus isolator (NL800A; Digitimer Ltd, Welwyn Garden City, UK). Once the expected activity was observed, the depth probe was gradually advanced ventrally, in 0.1 mm intervals, until the highest-amplitude population spikes were recorded by the central electrodes on the probe.

2.3. Induction of seizures by hippocampal electrical stimulation

Seizures were induced on demand by delivering a 2-s train of biphasic, charge-balanced square wave pulses, with a pulse width of 1 ms, to the stimulating electrode placed in the angular bundle of the perforant path at a frequency of 100 Hz using a Keithley 6221 current source (Keithley Instruments Ltd, Solon, OH, USA), in accordance with the hippocampal epileptic ADs model optimised for EIT recordings (Hannan, 2019) (Fig. 1a). At a current amplitude of 1.5 mA, these stimulus trains were consistently able to elicit epileptiform events with reproducible electrographic characteristics which could be recorded from the dentate gyrus in all animals. A minimum inter-train interval of 12 min allowed baseline activity to return following seizure induction and ensured that seizure patterns remained stable over the course of the experiment.

2.4. EIT hardware, data acquisition and protocols

The ScouseTom EIT system, comprising the actiCHamp 128-channel EEG amplifier (Brain Products GmbH, Gilching, Germany) and Keithley 6221 current source (Keithley Instruments Ltd, Solon, OH, USA), was used to obtain ECoG/LFP and tissue impedance measurements

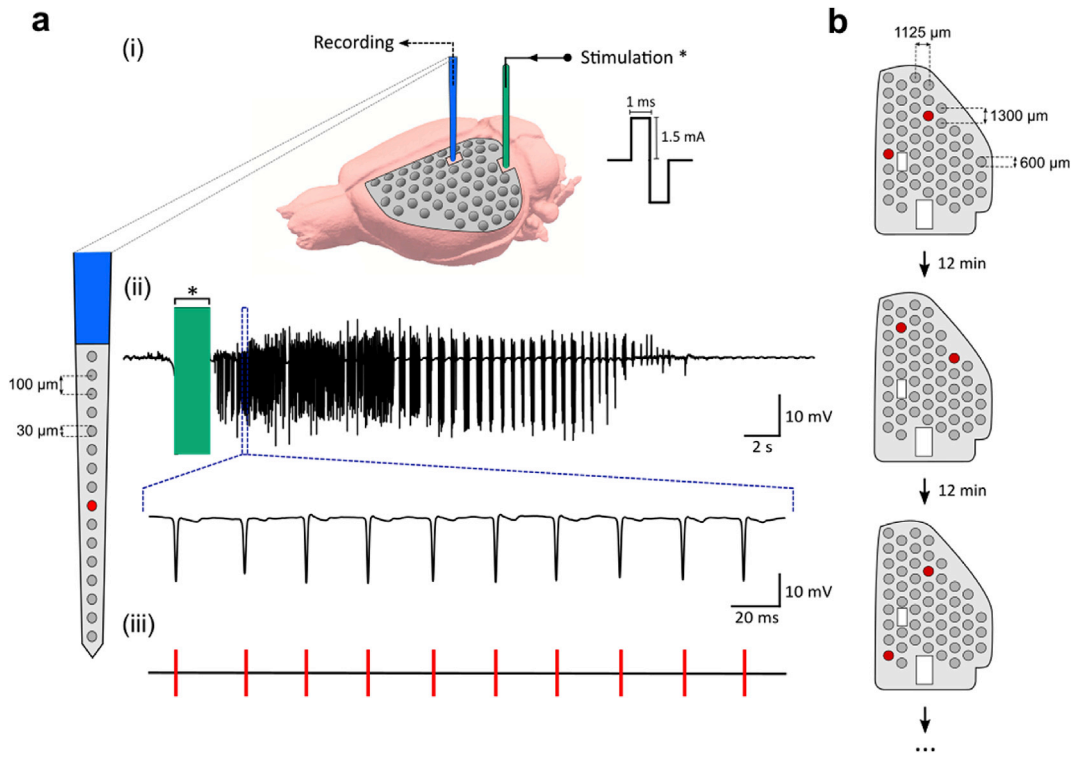

Fig. 1. Schematic of experimental setup. (**a**) The angular bundle of the perforant path was electrically stimulated with a 2-s train of 100 Hz biphasic square-wave pulses to induce seizures. Pulses were 1 ms in duration per phase and 1.5 mA in amplitude (**a**(i)). LFP recordings were made using a linear 16-channel depth probe implanted into the dentate gyrus, and a 54-electrode epicortical array was used to obtain ECoG and EIT recordings from the cortical surface. Using the LFP recording from the trigger channel marked in red (**a**(ii)), an event marker was set at the peak of each detected granule cell population spike during the seizure (**a**(iii)); these trigger markers were then used to construct averaged ECoG and impedance waveforms of a single ictal population spike per seizure. (**b**) During each imaging protocol, transfer impedances were recorded by injecting current through a different electrode pair on the 54-electrode epicortical array for each of ≥30 seizures; locations of and the distance between current-injecting electrodes were varied to ensure adequate sampling of the cortex and hippocampus. A 12-min rest period between stimulation series ensured that seizures remained stable during imaging protocols.

simultaneously (Avery et al., 2017). LFP data collected by the recording depth electrode contacts were passed through a unity gain headstage amplifier (HST/32o25-GEN3-36P-G1; Plexon, Dallas, TX, USA) prior to reaching the EEG amplifier. All recordings were made with respect to a reference electrode, comprising a Ag–AgCl plate that was 9 mm in diameter placed beneath the nuchal skin, and digitised at a sampling frequency of 25 kHz. For each EIT recording, a constant sinusoidal current, at a carrier frequency of 1.355 kHz and an amplitude of 100 µA, was injected through a single pair of electrodes on the 54-electrode array. Independent voltage measurements for the resulting current pattern were obtained from the remaining electrodes on the array. Each impedance recording contained the seizure, in addition to baseline periods of ≥10 s prior to stimulation and ≥30 s after the last ictal discharge.

A full EIT protocol for imaging hippocampal epileptiform activity comprised at least 30 independent impedance measurements and a different electrode pair on the epicortical array was used for current injection during each of the 30 induced seizures (Fig. 1b). The EIT current-injecting electrode pairs were manually switched in the 12-min recovery period in between seizures. As such, the LFP and ECoG data acquisition during these recordings, which included the pre- and post-ictal baseline periods, were unaffected by switching artefacts. The current-injecting electrodes in the EIT protocol were separated by 2.6–12.5 mm. Since the tissue penetrating depth of the injected current is dependent on the inter-electrode distance, the electrode-addressing sequence was determined using mathematical modelling to maximise the current density, and thus sensitivity to impedance changes, throughout the cerebral cortex and hippocampal formation in the left hemisphere (Faulkner et al., 2017). Due to the acute nature of the experimental setup and its time constraints, a subset of ≥30 independent current-injecting electrode pairs were randomly selected from this full theoretical protocol which comprised 53 electrode pairs. The electrode geometry and EIT protocol used provided a spatial resolution of ~300 µm in most of the neocortex and hippocampus; this value reflects the minimum distance between perturbations simulating epileptiform neural activity in the hippocampus at which the reconstructions can be distinguished, determined using an approach described previously (Aristovich et al., 2014; Aristovich et al., 2016).

2.5. *Experimental controls*

Control recordings were made to validate that the observed impedance changes were indeed due to the induced epileptiform activity. First, the 10-s baseline impedance recording prior to delivery of the stimulus train was assessed to confirm that the measured impedance response was not due to resting state cortical or hippocampal activity. Secondly, a full EIT protocol was performed post-mortem in two animals under the same experimental conditions as the *in vivo* imaging but with data collected after the animals had been culled; this eliminated the possibility that the impedance changes were due to artefacts caused by stimulation of the perforant path or the presence of the depth probe in the hippocampus. In addition, a minimum of three control LFP recordings were undertaken in each animal during seizures in the absence of EIT current injection prior to starting the EIT protocol. After visually assessing these LFP traces and comparing them to those of seizures recorded during the EIT protocol, it was confirmed that, as expected, continuous current injection at 100 µA and 1355 Hz did not alter the electrographic pattern of ictal discharges in the induced seizures.

2.6. Analysis of ECoG, LFP and impedance data

The recorded raw voltage measurements made from the available epicortical and depth electrodes contained the ECoG/LFP and impedance signals, which were extracted using different filter settings. The ECoG and LFP signals were obtained by application of Butterworth filters at 1 Hz (high-pass, first order) and 1 kHz (low-pass, fifth order), in addition to a 50 Hz notch filter (IIR, second order). Use of this 1 kHz low-pass filter eliminated any interference in the EEG recordings from the EIT current, which was a clean sine-wave injected at 1.355 kHz, and enabled continuous monitoring of ECoG and LFP traces of hippocampal seizures from all channels during data acquisition. The impedance signal was extracted by applying a ±500 Hz bandpass Butterworth filter (fifth order) around the 1.355 kHz carrier frequency, yielding a temporal resolution of 2 ms, and demodulating the signal using the Hilbert transform. The width of this bandpass filter ensured that any contamination of the EIT signal with noise due to EEG activity was minimal to yield an adequate SNR for imaging.

To enable imaging of the induced hippocampal ictal discharges from the cortical surface, averaging of the associated impedance changes was required. For this purpose, the channel displaying the highest-amplitude ictal discharges in the filtered LFP traces, which was consistent across seizures and animals, was selected as the trigger signal for subsequent spike detection and sorting. Detection and classification of ictal discharges was then performed in this trigger signal using an automated neuronal spike classification algorithm (Quiroga et al., 2004), which generated an array of trigger marker timings corresponding to the peak amplitudes of all detected ictal discharges (**Supplementary Information 1.3**). The negative-going granule cell population spike was the only type of spontaneous epileptiform discharge seen consistently during all seizures in all animals. This was defined as a sharp negative potential, <8 ms in duration, with a minimum local peak-to-peak amplitude of 2 mV, in accordance with the expected electrographic presentation of the ictal granule cell population spikes induced by the hippocampal epileptic ADs model (Bragin et al., 1997; Hannan, 2019). Trigger markers were set at the negative peaks of all detected high-amplitude population spikes with an inter-spike interval of ≥20 ms and verified by visual inspection (Fig. 1a). Only individual ictal spikes that lay within ±3 SD of the mean trace for all detected spikes in a given seizure were preserved for averaging.

The demodulated impedance signals from all epicortical electrode channels for each seizure were aligned with respect to the verified trigger markers. For each epicortical channel, the impedance change (dZ) associated with every repeatable population spike was averaged within recordings, resulting in a mean dZ trace per seizure. A 40-ms temporal window centred around the trigger marker, which encompassed the entire population spike in addition to pre- and post-spike baseline periods, was used for averaging. Time points with significant activity were identified across all channels by comparing the dZ value with the baseline dZ, defined as the mean amplitude during the first 5 ms of the 40-ms temporal window, using a paired *t*-test at a significance level of $\alpha = 0.01$. Current-injecting and disconnected channels were rejected from further analysis. In addition, the measured boundary voltages were processed to reject channels with no detectable physiological contribution, a requirement for accurate EIT image reconstruction of fast neural activity. Boundary voltages with a real component of <100 μV, or temporal noise of ≥1%, indicated a low SNR on the corresponding channels and so were rejected to avoid amplification of noisy data, in accordance with a previous in-house study which demonstrated that this approach results in improved image quality (Packham, 2013). Channels were also rejected by thresholding according to the baseline SD: within the time period of significant activity, significant channels were defined as those with dZ greater than three times the baseline SD and were preserved (Packham, 2013). dZ measurements from remaining channels, which constituted 76.0 ± 8.3% of the total number of channels ($n = 162$ seizures, $N = 5$ rats), were collated across seizures to produce an image of a single averaged ictal spike. All data are presented as mean ± SD.

2.7. Tomographic reconstruction of hippocampal impedance changes

EIT images of averaged ictal granule cell population spikes were produced using ≤1560 processed impedance traces, which comprised ≤52 voltage measurements (54 electrode channels minus current-injecting, disconnected and low SNR channels) for each of 30 independent current injections. The forward solution involves prediction of boundary voltages resulting from a defined current injection protocol. This was calculated for a given EIT protocol on an anatomically realistic finite element method (FEM) mesh of the rat brain, generated from MRI images obtained in 21 adult Sprague-Dawley rats (Nie et al., 2013) and comprising 2.9 million tetrahedral elements, using the PEITS forward solver with the complete electrode model (Jehl et al., 2015). The complete electrode model specifies a set of boundary conditions which have been experimentally validated for accurately modelling the interface between the highly conductive surface electrodes and the considerably less conductive underlying tissue (Boverman et al., 2007). The positions of the epicortical electrodes on the mesh were altered to match their positions during a given experiment, as determined by the electrode coordinates and photographs taken after implantation of the array. Measurements were obtained with respect to a reference electrode, 9 mm in diameter, placed over the dorsal surface of the cerebellum. Tissue conductivity was assumed to be isotropic throughout the cerebral grey matter (0.3 Sm^{-1}) and white matter (0.15 Sm^{-1}), and the conductivity of the cerebrospinal fluid (CSF) was set at 1.79 Sm^{-1} (Ranck, 1963; Baumann et al., 1997; Latikka et al., 2001) (compiled from literature by Horesh (2006)). The time-difference EIT approach was employed for imaging, based on the principle that modelling errors are largely cancelled out when a reference baseline measurement is subtracted from the data measurement (Brown, 2003). As such, the overall effect of the chosen conductivity values for the grey matter, white matter and CSF in the mesh of the rat brain on the final reconstructed images is minimal (Brown, 2003; Jehl et al., 2016). An inversion of the resulting Jacobian matrix was used to solve the inverse problem. To prevent the inverse crime and reduce computational time (Lionheart, 2004), reconstructions were performed on a coarse hexahedral mesh containing approximately 80,000 elements, 300 μm in length. Zeroth-order Tikhonov regularisation with noise-based correction was applied after selection of the regularisation parameter through generalized cross-validation (Tikhonov et al., 1995; Aristovich et al., 2014). Images were reconstructed at 1 ms time-steps for the entire temporal window of the average spike-related impedance change.

The reconstructed conductivity changes in each hexahedral voxel were corrected using a previously described noise-based correction approach and expressed as t-score (δσ) for visualisation (Aristovich et al., 2014). This involves dividing the reconstructed conductivity values by the computed SD of the estimated conductivity change, due to random Gaussian noise in the voltage measurements, for each hexahedron.

2.8. Analysis of reconstructed images

The reproducibility of images across animals was assessed quantitively with population statistics by labelling active voxels, defined as those with $\delta\sigma \geq 3$ ($p < 0.01$) in each reconstruction, using a binomial mask. The volume of common active voxels with $p < 0.03125$ (0.5^5) across all five rats was then visualised. In each image, the centre of mass of activity was calculated at the time of maximal activity by thresholding the reconstruction at 50% of the maximal δσ (full width at half maximum; FWHM) and determining the largest connected cluster of active voxels in 4D. The mean centre of mass was determined across animals to estimate the localisation accuracy of reconstructions with respect to the expected location of maximal activity within the dentate gyrus, at which the central electrodes on the linear 16-channel neural depth probe were targeted (AP = −4.0, ML = 2.5, DV = 2.8 mm). The

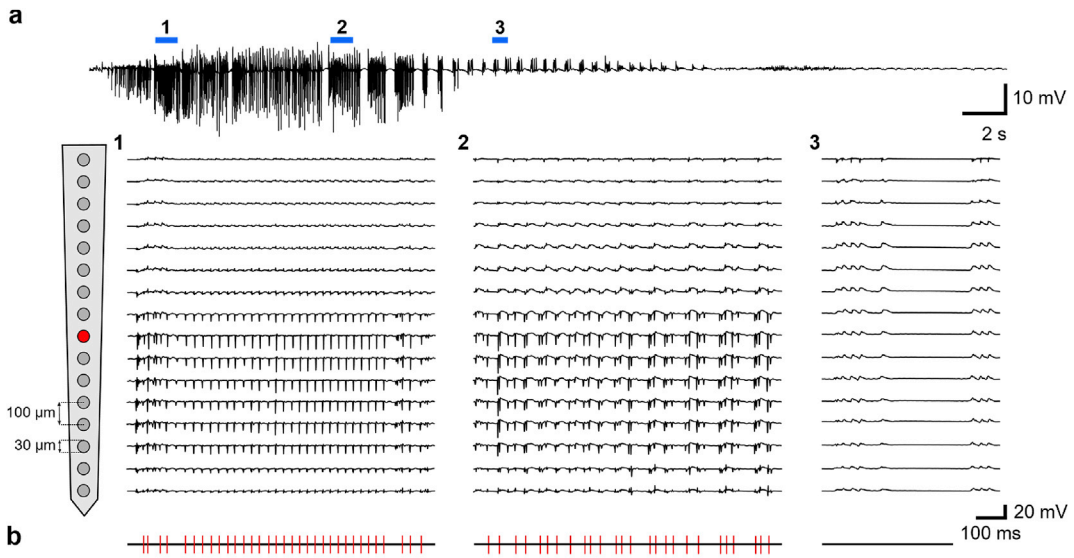

Fig. 2. LFP recording of typical hippocampal seizure induced by electrical stimulation of the perforant path. (**a**) A representative seizure induced by stimulation of the perforant path is displayed; the start of the seizure epoch corresponds to the end of the 2-s stimulation period. Three epochs, obtained at different stages of the seizure at the times indicated and recorded by a 16-channel depth probe implanted into the dentate gyrus, are provided. The seizure initially contains repeatable trains of granule cell population spikes (epoch 1). In the second half, shorter bursts of population spikes can be seen, some of which are superimposed on fEPSPs (epoch 2). At the tail-end of the seizure, fEPSPs are seen with no population spikes (epoch 3). The trigger channel on the depth probe, from which the highest-amplitude population spikes were recorded, is marked in red. (**b**) Trigger markers for all population spikes detected by the spike sorting algorithm and deemed sufficiently repeatable for averaging are displayed for the three epochs. For all induced seizures, the majority of trigger markers were set during the first half of the seizure.

reconstructed activity and centre of mass positions were also qualitatively evaluated with respect to a detailed anatomical atlas of the rat brain (Paxinos and Watson, 2013) to determine regions within the hippocampal formation that were implicated in the ictal activity.

2.9. Data and code availability

The data presented in this article and code used for analysis are available from the corresponding author on request.

3. Results

3.1. Electrographic features of induced hippocampal seizures

The induced seizures comprised a characteristic pattern of focal, rhythmic and high-amplitude (2–15 mV) granule cell population spikes at 30–50 Hz, which were recorded locally from the dentate gyrus immediately after stimulating the perforant path (Fig. 2). All seizures began with a continuous series of negative-going population spikes which subsequently evolved to population spike bursts, occasionally superimposed on positive-going fEPSPs during the second half of the seizure. These population spike bursts were sometimes followed by runs of fEPSPs with the absence of population spikes during the end of the seizure; such discharges were excluded from further analysis. Across all animals, the mean seizure duration was 28.3 ± 9.5 s, and the mean number of ictal spikes used for averaging was 394 ± 86 ($n = 162$ seizures, $N = 5$ rats).

3.2. Characterising the impedance response to hippocampal ictal spikes

Following spike detection and classification, the LFP, ECoG and impedance recordings for individual ictal spikes within each seizure were averaged together. Averaged ECoG recordings displayed a positive-going spike component in phase with the averaged LFP recording of the ictal spike (Fig. 3a and b). In the averaged impedance recordings, a significant dZ above baseline noise level that was in phase with the LFP recording of the ictal spike was observed in response to 32.7 ± 2.5% of the total number of EIT current injections across all protocols ($p < 0.01$, $n = 162$ seizures, $N = 5$ rats, paired t-test). When such a dZ response was observed, this was characterised by a sharp maximal impedance decrease of 0.041 ± 0.013%, lasting <8 ms, which occurred in phase with the peak of the spike as determined by LFP and ECoG recordings (Fig. 3c; $n = 53/162$ seizures, $N = 5$ rats). The topographic arrangements of representative LFP, ECoG and dZ traces across electrode arrays during an averaged hippocampal ictal spike are displayed (Fig. 4). As expected, the magnitude of the maximum dZ for each EIT recording depended on the spatial arrangement of current-injecting electrodes on the epicortical array, which determined the current density and sensitivity through the underlying cerebral tissue (**Supplementary Information 2.1**).

3.3. EIT images of hippocampal ictal spikes and statistical analysis

The processed dataset from each rat was reconstructed into an EIT image of the fast neural impedance response during an averaged ictal granule cell population spike, the primary component of seizures induced by the hippocampal epileptic ADs model. EIT images were reconstructed every 1 ms and spanned −15 to 20 ms, where 0 ms corresponds to the peak amplitude of the spike in the LFP recording. In all animals, the earliest time point at which significant activity could be observed in the EIT images was −2 ms relative to this peak LFP response (Fig. 5; $n = 162$ seizures, $N = 5$ rats). This activity arose within the structural centre of the dentate gyrus in the AP axis. Voxels with maximal δσ were localised to an AP coordinate of −4.0 mm relative to bregma, corresponding to the position at which the neural depth probe was implanted. Coronal sections obtained at this position revealed that activity lay ventral to the hippocampal fissure and encompassed the dorsal two-thirds of the dentate gyrus, including the granule cell, molecular and polymorphic layers and the hilus, in addition to the medial-most segment of the CA3 hippocampal field (Fig. 6). The volume of active voxels increased between −2 and 0 ms as the peak LFP and dZ amplitudes were reached, spreading medioventrally whilst remaining within the dentate gyrus, (Figs. 5 and 6). Significant activity was not observed at 2 ms or later.

Application of a binomial mask revealed a spatially distinct region of common active voxels within the dentate gyrus across all animals during

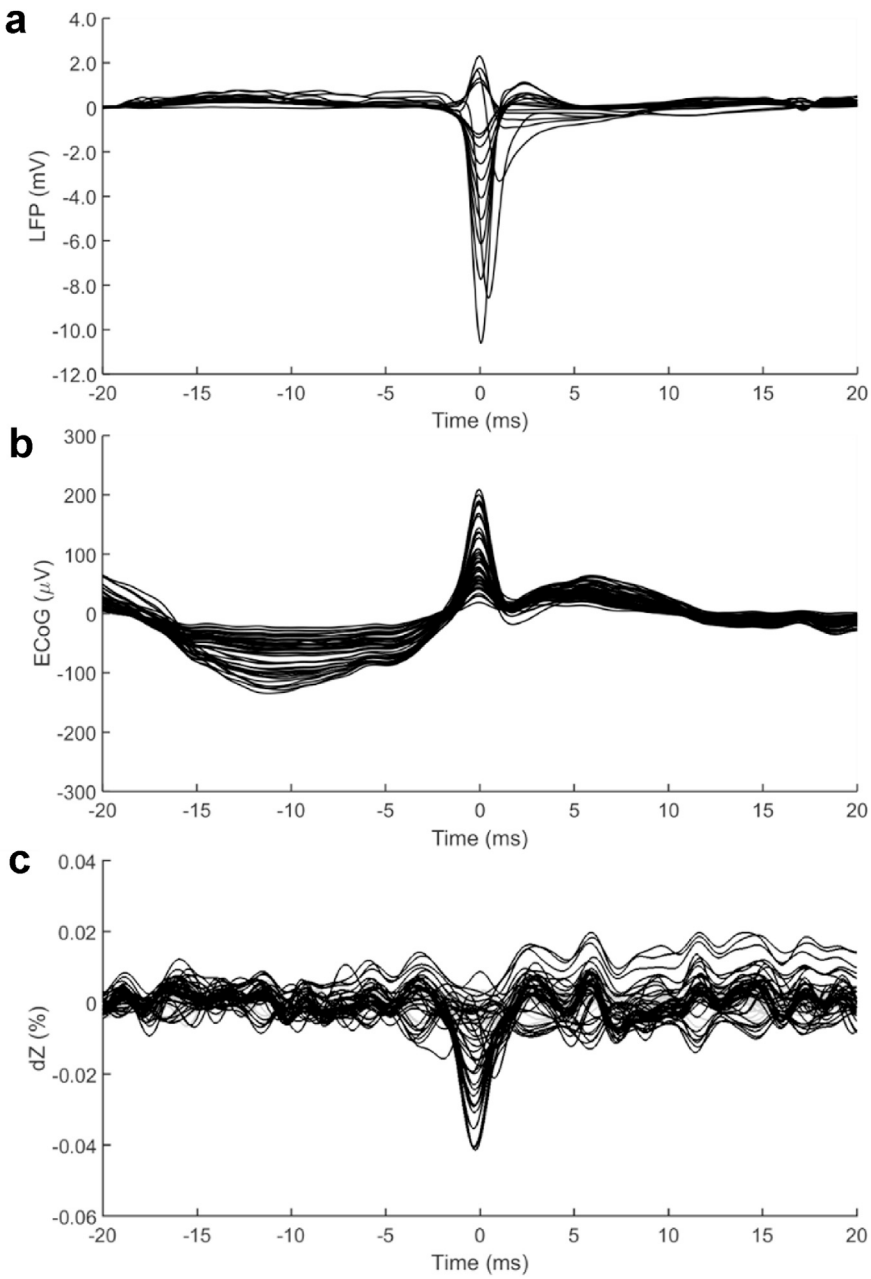

Fig. 3. Spatial and temporal features of LFP, ECoG and impedance responses during a hippocampal ictal spike. Representative examples of LFP (**a**), ECoG (**b**) and impedance (dZ) (**c**) recordings of an averaged ictal granule cell population spike from a single seizure. The LFP traces were recorded by the 16-channel neural depth probe implanted in the dentate gyrus, and ECoG and dZ traces were recorded with the 54-electrode epicortical array. The maximal ECoG amplitude of the spike (**b**), measured from the cortical surface, was consistently two orders of magnitude smaller than that recorded locally with the LFP electrodes (**a**), indicating that the ictal spikes indeed originated within the hippocampus.

the hippocampal ictal spike which matched the location of reconstructed δσ in individual rats (Fig. 7; $p < 0.03125$, $n = 162$ seizures, $N = 5$ rats). Control recordings further verified that the observed activity was not artefactual; baseline ($n = 162$ recordings, $N = 5$ rats) and dead controls ($n = 60$ recordings, $N = 2$ rats) showed no significant focal or diffuse activity when processed and reconstructed with the same methods as those for the induced hippocampal seizures.

The mean centre of mass of the peak activity, observed at 0 ms, was: AP = −4.1 ± 0.2 mm, ML = 2.4 ± 0.3 mm, and DV = 3.2 ± 0.4 mm from the surface of the cerebral cortex; AP and ML are given with respect to bregma (Table 1; $n = 162$ seizures, $N = 5$ rats). This position corresponds to the medial segment of the granule cell layer within the dentate gyrus. The distance of this reconstructed centre of mass from the anticipated location of maximal activity, at which the central electrodes on the linear 16-channel neural depth probe were targeted (AP = −4.0, ML = 2.5, DV = 2.8 mm from the cortical surface, assuming no swelling of the cerebral cortex following the craniotomy and durotomy), was 100 μm in the AP and ML axes, and 400 μm in the DV axis. Therefore, a localisation accuracy of ≤400 μm was achieved in reconstructions.

4. Discussion

In this work, we evaluated the feasibility of imaging the fast neural impedance response to ictal epileptiform discharges in the rat hippocampus with EIT, using non-penetrating epicortical electrodes. Averaged ictal granule cell population spikes, induced by the hippocampal epileptic ADs model, consistently displayed a sharp impedance decrease in phase with the peak of the spike as observed in the corresponding LFP recordings. EIT images of this impedance decrease during hippocampal ictal spikes could be reconstructed reproducibly with a resolution of 2 ms and ~300 μm. Images revealed a focus of neural activity localised to the dentate gyrus between −2 ms and 0 ms, relative to the peak of the spike in the LFP recording. The reconstructions were well-aligned, both spatially and temporally, to LFPs recorded with a neural depth probe implanted into this region. Centre of mass analysis of images demonstrated that a localisation accuracy of ≤400 μm could be achieved in

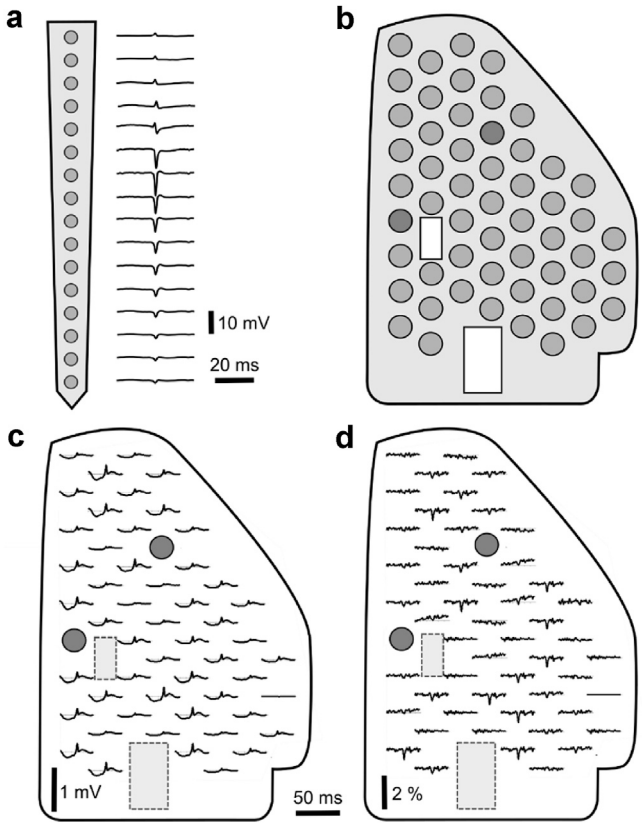

Fig. 4. Topographic arrangement of LFP, ECoG and impedance responses during a hippocampal ictal spike. (**a**) Representative averaged LFP traces of an ictal granule cell population spike recorded with the 16-channel neural depth probe are displayed. (**b**) A schematic of the 54-electrode epicortical array used to obtain ECoG and impedance recordings; the EIT current-injecting electrode pair is indicated (red). The spatial arrangement of a representative example of ECoG (**c**) and dZ (**d**) traces across this epicortical array. Channels with excessive noise have been removed and are shown in the array as flat traces.

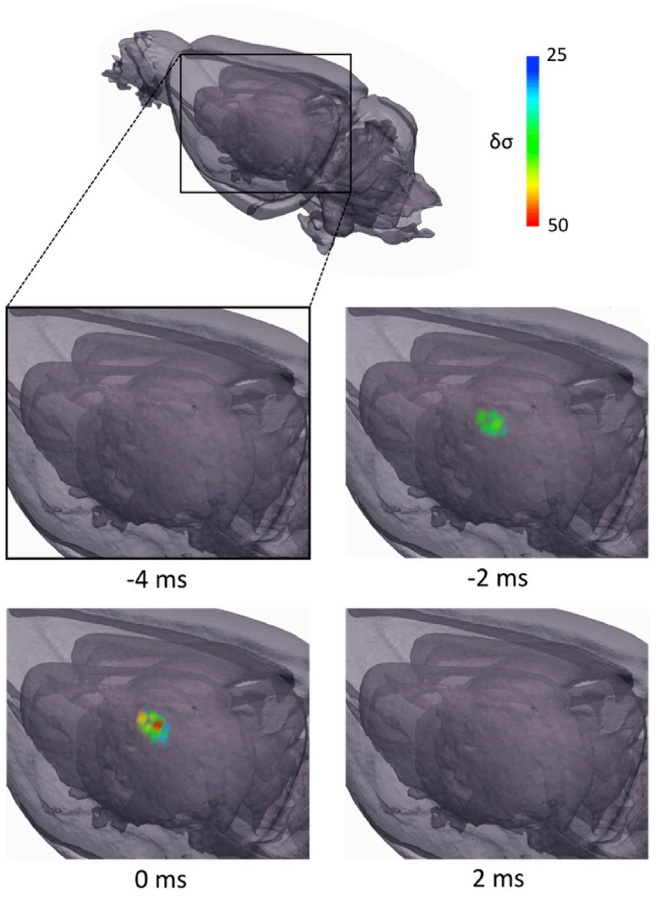

Fig. 5. EIT image showing fast neural impedance changes during a hippocampal ictal spike. The sequence of images, obtained every 2 ms over a total time period of 7 ms, reveal an early focus of activity localised to the dentate gyrus at −2 ms. A subsequent medioventral propagation of activity is observed at 0 ms, at which point the activated volume reaches a maximum. At 2 ms and beyond, no active voxels were observed. Time is given with respect to the peak amplitude of the population spike in the LFP recording and δσ represents t-score of conductivity changes.

reconstructions. This work represents the first experimental evidence of the ability of EIT to image fast electrical activity during neuronal depolarisation in subcortical structures from the surface of the cerebral cortex.

4.1. Technical considerations

The ictal granule cell population spikes imaged here were induced by the hippocampal epileptic ADs model, in which focal epileptiform events are elicited on demand by electrically stimulating the perforant path. This enabled total control of the EIT protocol for imaging. The hippocampal epileptic ADs model is limited in its lack of cell-type specificity and thus inability to influence the firing characteristics of specific neuronal groups (Kandratavicius et al., 2014). As such, it does not provide the most realistic representation of human mesial TLE compared to certain acute or chronic chemical epilepsy models. However, this proof of concept study was aimed at assessing whether it was feasible to use EIT to image subcortical neural activity using non-penetrating epicortical electrodes and evaluating the technical accuracy of the technique. Therefore, modelling specific pathophysiological features of clinical epilepsies was beyond the scope of this work. Nonetheless, since EIT was shown to be capable of imaging hippocampal neural activity from the cortical surface, we plan to undertake future studies to assess the possibility of imaging epileptiform activity in clinically representative animal models that produce spontaneous seizures with more variable electrographic presentations.

A limitation of the proposed method in its current state of development relates to the need for averaging ictal discharges within seizures, which is necessary to improve the SNR for imaging due to the low magnitude of fast neural impedance changes associated with individual discharges (Vongerichten et al., 2016; Hannan et al., 2018a). However, we utilised a spike classification algorithm which identified ictal population spikes exhibiting a high degree of electrographic repeatability based on strict criteria including waveform shape, amplitude, duration and inter-spike interval (Quiroga et al., 2004). Furthermore, LFP recordings from the 16-channel linear depth probe implanted into the dentate gyrus to validate the presence and localisation of the induced ictal spikes showed that the amplitude and electrographic pattern of spikes recorded by any given electrode along the depth of the probe remained stable over the course of the seizure. This confirmed that the induced ictal spikes were spatially confined to a consistent location during each seizure, as is expected in the hippocampal epileptic ADs model (Bragin et al., 1997). Therefore, overall, it can be assumed that averaging of the impedance change associated with such repeatable population spikes within seizures is unlikely to have considerably distorted the spatiotemporal features of the impedance responses to individual spikes. As such, images of such neural events obtained with this approach are representative of the true location of the epileptogenic zone.

The presence of the 16-channel linear silicon probe used for LFP recordings from the dentate granule cell layer was not taken into consideration when computing the forward solution. Although the probe itself was insulated, the 16 iridium contacts, each 100 μm in diameter, were

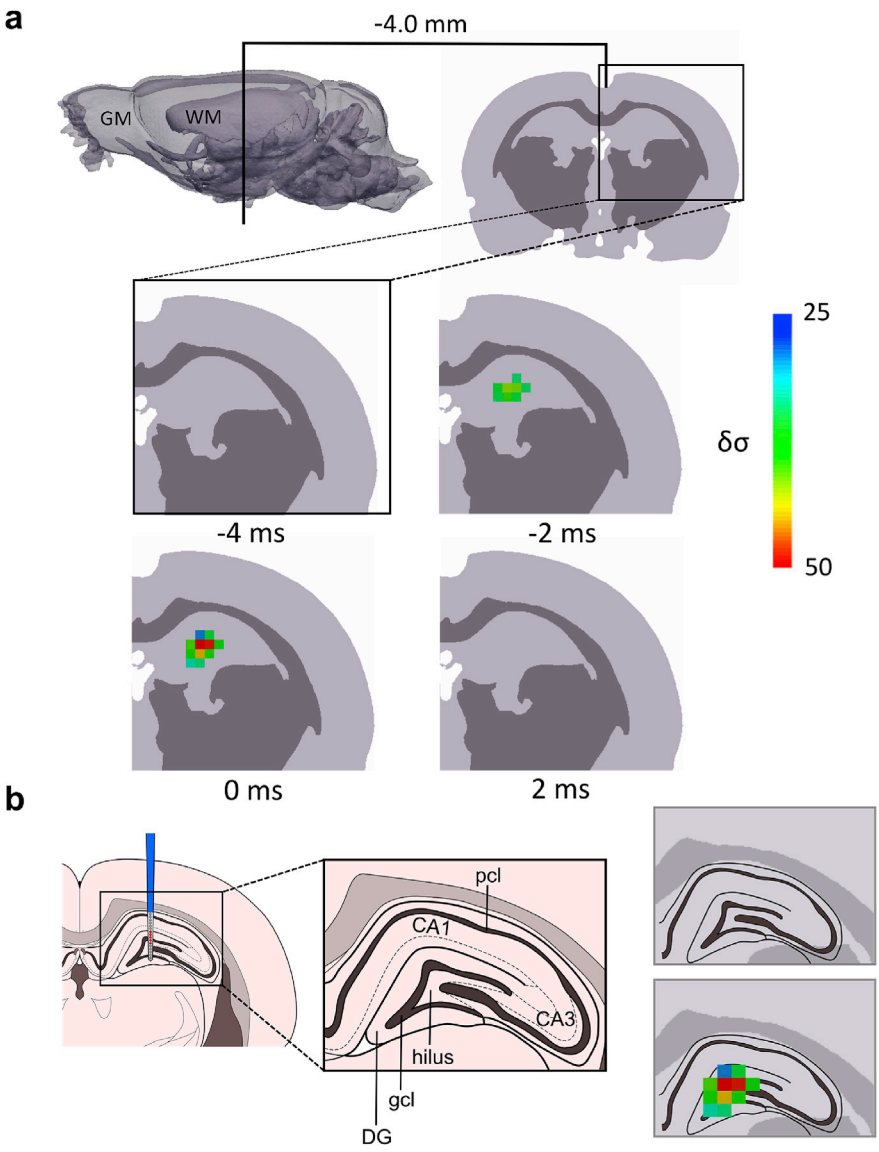

Fig. 6. Mediolateral and dorsoventral localisation of reconstructed ictal spike-related impedance changes. (**a**) Coronal sections transecting the maximally activated voxels in the reconstructed image (4.0 mm posterior to bregma) were obtained at four time points from −4 to 2 ms, with respect to the peak LFP response of the ictal spike. An increase in the activated volume in the medioventral direction can be observed between −2 and 0 ms. (**b**) The peak δσ, observed at 0 ms, is superimposed on a coronal section displaying the hippocampal formation at 4.0 mm posterior to bregma, adapted from Paxinos and Watson's stereotactic atlas of the rat brain (Paxinos and Watson, 2013). The position of the 16-channel neural depth probe is indicated for reference (left). The reconstructed activity was confined to the dentate gyrus in the dorsoventral axis and encompassed the most medial segment of the pyramidal cell layer in the CA3 field. δσ represents t-score of conductivity changes. GM, grey matter; WM, white matter; DG, dentate gyrus; gcl, granule cell layer; pcl, pyramidal cell layer.

more conductive than the cerebral tissue into which they were implanted and so may have altered the distribution of current resulting from current injection through certain pairs of epicortical electrodes in the EIT protocol. This in turn would influence, to varying degrees, the spatial sensitivity profile of different current-injecting electrode pairs. However, because time-difference EIT data was used for reconstructions, based on the principle that most geometric and system-related errors cancel out when a reference baseline measurement is subtracted from the data measurement (Brown, 2003), the effects of such modelling errors on the final image are minimised. Additionally, the presence of a statistically significant spatially distinct region of common active voxels reconstructed to the expected location across rats ($p < 0.03125$, $N = 5$ rats), which was not observed in baseline or dead controls subjected to the same EIT protocols and experimental setup, lends support to the view that the reconstructed activity was not artefactual. Nevertheless, modelling the presence of depth electrodes in the forward solution in the future may improve the quality and localisation accuracy of reconstructions.

4.2. Comparison of findings to literature and implications for understanding mechanisms of ictal events

The sharp impedance decrease visible during averaged ictal granule cell population spikes was in phase with the corresponding LFP recordings of this activity obtained from the dentate granule cell layer. This impedance response can thus be attributed to the alterations in extracellular concentrations of potassium and calcium ions that underlie this spiking activity (Pan and Stringer, 1997). The amplitude of this hippocampal fast neural impedance change as recorded from the cortical surface (~0.04%) was one order of magnitude smaller than that observed previously during ictal and interictal spikes induced in the cerebral cortex (~0.3%) (Vongerichten et al., 2016; Hannan et al., 2018a). Despite its lower absolute magnitude, the signal could still be detected in averaged impedance traces and EIT images due to the fact that it was possible to use more ictal spikes for averaging within a given hippocampal seizure (394 ± 86 ictal spikes; $n = 162$ seizures, $N = 5$ rats) compared to a cortical seizure (46 ± 19 ictal spikes; $n = 168$ seizures, $N = 5$ rats (Hannan et al., 2018a)). This was because ictal spikes induced by the hippocampal epileptic ADs model were shorter in duration and occurred at a higher frequency than the cortical epileptiform discharges described previously (Hannan et al., 2018a). As such, the resulting SNR was adequate to enable imaging of epileptiform activity in the hippocampus from the surface of the cortex.

The reconstructed activity occurred from −2 to 0 ms relative to the peak amplitude of the averaged population spike in LFP recordings and, at both time points, was spatially confined to the dentate gyrus and most

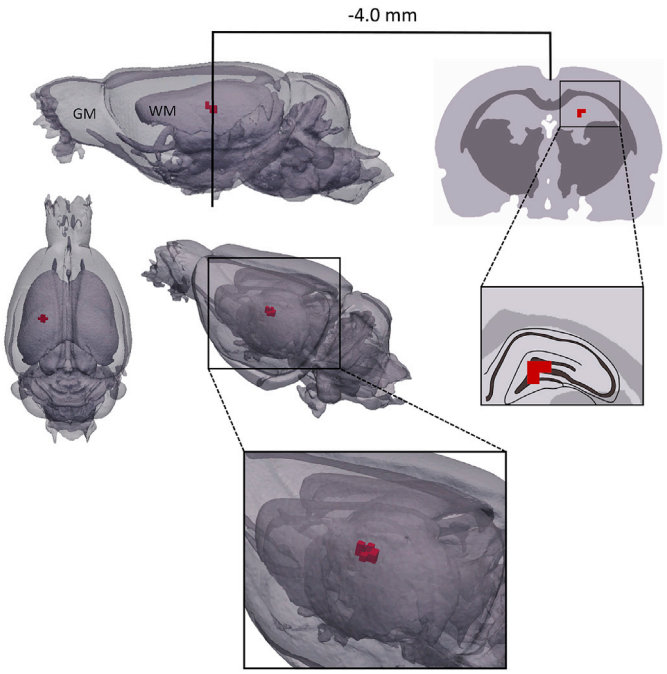

Fig. 7. Population statistics of EIT images. Sagittal, dorsal and posterolateral views (left) of common active voxels (marked in red) in the reconstructed δσ across rats at 0 ms relative to the peak amplitude of the ictal population spike in the LFP recording ($p < 0.03125$, $N = 5$). A coronal section transecting the maximally activated region of the dentate gyrus, obtained at 4.0 mm posterior to bregma, is shown (right). The magnified area of the hippocampal formation reveals that common active voxels are confined mainly to the granule cell layer of the dentate gyrus. GM, grey matter; WM, white matter.

medial segment of the CA3 field (Fig. 6). Between −2 and 0 ms, the active volume spread in the medioventral direction and encompassed a larger portion of the dentate gyrus. The localisation of the reconstructed fast neural impedance change to the dentate gyrus is in agreement with the known electrophysiology of population spikes induced by perforant path stimulation, which represent the synchronisation of action potentials from populations of dentate granule cells (Andersen et al., 1971; Bragin et al., 1997). In addition, the presence of active voxels within the medial CA3 region across all animals (Fig. 7) may indicate the excitation of CA3 pyramidal neurons by dentate granule cells via the mossy fibre pathway. As these pyramidal neurons can in turn excite granule cells, the EIT images may reflect activation of this positive feedback loop that underlies the rhythmic population spikes observed in this epilepsy model (Andersen et al., 1971; Scharfman, 1994; Scharfman, 1996; Bragin et al., 1997).

For a complete understanding of the underlying mechanisms of epileptiform discharges, it is preferable to image neural activity during such events with high spatiotemporal resolution over large volumes of the intact brain. A high spatial resolution (20–50 μm) may be achieved with optical imaging methods, using either chemical or genetically-encoded calcium indicators; however, these have a limited sampling volume of ~1 mm^3 and penetration depth of ~1 mm (Stosiek et al., 2003; Hillman, 2007; Ahrens et al., 2013; Kondo et al., 2017). Similarly, use of high-density penetrating microelectrode arrays for LFP recordings can provide a high spatiotemporal resolution but such electrode arrays are only able to sample neural activity over several cubic millimetres (Kajikawa and Schroeder, 2011). Additionally, due to their inherently invasive nature, microelectrode arrays can cause local tissue disruption. Although fast neural EIT is limited in its spatial resolution of ~300 μm, it can image over larger volumes than these techniques (Aristovich et al., 2016; Hannan et al., 2018a), has a superior penetration depth of at least >3 mm in the rat brain, and uses non-penetrating surface electrodes, which ensures that any neural circuits implicated in epileptogenesis

Table 1
Centre of mass of peak activity in reconstructed images across animals. Anteroposterior (AP), mediolateral (ML) and dorsoventral (DV) coordinates for the centre of mass positions at 0 ms, the time point of maximal reconstructed activity, for each of the five rats. AP and ML values are given with respect to bregma, and DV values are given from the surface of the cerebral cortex. The mean centre of mass was calculated to provide an indication of the localisation accuracy of reconstructions.

	Centre of mass (mm)		
Rat	AP	ML	DV
1	−4.2	2.7	3.2
2	−3.9	1.8	2.9
3	−4.2	2.4	3.8
4	−4.5	2.7	3.5
5	−3.9	2.4	2.6
Mean	−4.1	2.4	3.2
SD	0.2	0.3	0.4

remain intact during imaging. An alternative approach is to image the epiphenomenal local increase in metabolism and blood flow due to neural activity using functional MRI (Heeger and Ress, 2002). A variant of this technique, diffusion MRI, images changes in local water diffusion which are closely linked to neural activity (Tsurugizawa et al., 2013). Whilst these techniques enable non-invasive imaging of these secondary events over large volumes of the brain, the neurovascular coupling mechanisms and exact relationship between water diffusion or cell swelling and neural activity in epileptogenesis are poorly understood (Logothetis et al., 2001; Olsson et al., 2006; Ma et al., 2013; Renvall et al., 2014; Ullah et al., 2015). Since ictal events are defined as periods of abnormally synchronous neuronal activity, it is desirable to image this activity directly to truly understand the pathophysiology of these events, which can be achieved with fast neural EIT as presented in this study. Given the range of advantages and limitations of the abovementioned imaging modalities, the specific research question will dictate which should be utilised in a given study. Overall, the ability of EIT to image fast neural impedance changes on the mesoscopic scale in long-range neural networks over large volumes of cerebral tissue renders it a useful technique for mapping functional connectivity between cortical and subcortical structures in the rat brain. This would be particularly relevant, for example, for *in vivo* studies aimed at understanding the altered patterns of functional connectivity between the entorhinal cortex and hippocampus in mesial TLE (Burianová et al., 2017; Janz et al., 2017).

4.3. Potential clinical applications for fast neural EIT

This study demonstrated that the depth sensitivity of fast neural EIT to epileptiform activity extends to over a third of the depth of the rat brain (>3 mm). If translated to the clinical setting, the depth sensitivity of this method would scale up to enable imaging of neural activity in at least the outer third of the human brain, provided that a similar arrangement of epicortical electrodes is implemented. Clinically used subdural grids can contain as many as 64 electrodes, each of which is typically 2–4 mm in diameter (Wyler, 1992; Diehl and Lüders, 2000; Voorhies and Cohen-Gadol, 2013). Therefore, to achieve the current density of 354 Am^{-2} that enabled successful EIT imaging of hippocampal epileptiform activity in the present study, current would need to be applied through these subdural electrodes at an amplitude of 1.11–4.45 mA. The proportionally larger electrodes, higher amplitude of EIT current and greater electrode coverage would all contribute to a penetration depth that is proportionately comparable to that in the *in vivo* setup in the rat. As such, our proposed methodology is expected to enable imaging of fast neural impedance changes during epileptiform discharges that occur at least as deep as the human hippocampus. Another procedure that involves current application through these subdural electrodes in humans is cortical stimulation for functional brain mapping, in which current is applied at amplitudes up to 20 mA in brief (≤10 s) trains of biphasic

square wave pulses (So and Alwaki, 2018). These cortical stimulation protocols can sometimes induce immediate functional alterations in activity (Lesser et al., 2010). The possibility, albeit small, that this could occur in response to injecting EIT current must be addressed as it would be problematic for monitoring epileptic events. The threshold intensities for such functional alterations in response to cortical stimulation protocols vary widely between patients and different brain regions within the same patient (Pouratian et al., 2004; Lesser et al., 2010; Corley et al., 2017). Therefore, prior to undertaking EIT recordings, an initial testing stage should be conducted in each patient to definitively confirm that applying EIT current at the amplitude required to achieve a current density of 354 Am^{-2} (1.11–4.45 mA for 2–4 mm diameter subdural electrodes, respectively) does not cause such functional alterations in activity. If any such changes are observed, which is unlikely based on a previous *in vivo* assessment of the effect of EIT current at this current density on neural activity (Oh et al., 2011), then the amplitude of current for EIT measurements can be decreased accordingly in 0.5 mA increments (So and Alwaki, 2018). The amplitude of ictal spikes in the EEG recordings will depend on the type of epilepsy, the location of the seizure foci and the spatial configuration of recording electrodes with respect to this. Therefore, the threshold for detection of ictal spikes in the clinical setting, for the purpose of averaging the associated fast neural impedance changes to increase SNR for imaging, would need to be determined on a case-by-case basis by considering the amplitude of ictal activity with respect to the baseline noise.

The use of subdural electrode grids or strips in patients with mesial TLE is typically reserved for indications of multifocal epilepsy, particularly if seizure foci are present in eloquent regions of the cortex to enable cortical stimulation mapping, and those in which seizures are generated by an indeterminate epileptogenic zone (Lesser et al., 1987; Awad et al., 1991; Diehl and Lüders, 2000; Javidan, 2012). EIT may be used in such instances as an adjunct imaging modality to the conventionally used inverse source localisation methods based on ECoG recordings (Dümpelmann et al., 2012). Although the inverse problem in the two techniques is mathematically similar, EIT has the advantage of a unique solution to the inverse problem in contrast to source reconstruction methods, in which multiple current models may fit the recorded data (Somersalo et al., 1992; Jatoi et al., 2014). Additionally, it is possible to obtain more independent measurements for the same number of electrodes with EIT compared to ECoG ($O(n^2)$ versus $O(n)$, respectively, for n electrodes), since transfer impedances are recorded for every independent current injecting electrode pair in the EIT protocol, thus increasing the spatiotemporal information utilised for image reconstruction (Aristovich et al., 2018). Furthermore, inverse source localisation is limited as epileptic discharges may not have electroencephalographic correlates if they originate from sources that are oriented tangentially to the scalp or extend over sulci or gyri with opposing source orientations, leading to the selective cancellation of signals without reaching surface electrodes (Lüders, 2008; Ahlfors et al., 2010; Schomer and Lopes da Silva, 2010; Hunold et al., 2016). With EIT, on the other hand, any such cancellation of positive and negative fields is negligible as impedance changes due to neural activity are independent of underlying source orientation (Aristovich et al., 2018). The main limitation of EIT relates to the need for averaging due to the low magnitude of fast neural impedance changes measured on the cortical surface whereas the SNR of ECoG recordings is higher and permits real-time signal classification. The two techniques have been directly compared in several studies which demonstrated that EIT is able to provide a greater localisation accuracy than inverse source localisation (Aristovich et al., 2018; Witkowska-Wrobel et al., 2018; Avery et al., 2019). Considering the respective advantages and limitations of these methods, use of EIT as a complementary diagnostic tool to inverse source localisation would provide additional data using the same configuration of pre-implanted electrodes and without altering clinical workflows, which can increase the accuracy with which the epileptogenic zone is localised and ultimately improve surgical outcome.

Another promising avenue for the clinical translatability of EIT is the possibility of performing EIT protocols by injecting current through intracranial depth electrodes which are often implanted in or around anticipated seizure foci, as an alternative to subdural electrode arrays, for determining the extent of the epileptogenic zone in patients with refractory epilepsy (Spencer, 1981; Pillay et al., 1992; Diehl and Lüders, 2000). This method, which was shown to be feasible in a recent simulation study (Witkowska-Wrobel et al., 2018), would increase the current density, and thus sensitivity to impedance changes, in specific regions of interest likely to be implicated in the generation of epileptic events in these patients. The magnitude of the measured impedance responses is therefore expected to be larger which may mitigate the need for averaging epileptic discharges to obtain an adequate SNR for imaging. Furthermore, use of a parallel EIT system employing frequency-division multiplexing for clinical recordings would avoid the need for switching of current-injecting electrodes and thus eliminate the possibility of introducing any low-frequency switching artefacts into continuous EEG recordings (Dowrick et al., 2015; Avery et al., 2019). A parallel EIT system in which multiple current sources operate simultaneously at different carrier frequencies is currently under development for future clinical use.

5. Conclusion

This work has demonstrated the ability of EIT to image fast electrical activity during epileptiform discharges induced by a rat model of hippocampal epilepsy, with a resolution of 2 ms and ~300 μm, using non-penetrating electrodes implanted on the cortical surface. The depth sensitivity of EIT for imaging epileptiform neural activity with epicortical electrodes has therefore been shown to extend to the hippocampus, corresponding to a penetration depth of at least >3 mm. We are currently developing methods for evaluating the feasibility of imaging such activity in deeper structures, such as the thalamus, using a similar approach. In addition, there are several avenues for improving the practicability of this technique for use as a standard neuroimaging tool, which are currently being investigated. For example, optimising the EIT protocol to maximise current density in a region of interest, if known, can reduce the number of neural events required for imaging and development of a parallel EIT system may enable single-shot imaging of ictal activity from individual seizures (Dowrick et al., 2015; Faulkner et al., 2017). Future work should focus on utilising the strengths of EIT as an imaging modality, which include its ability to image neural activity at the mesoscopic scale over large volumes, to delineate the spatiotemporal dynamics of long-range cortico-hippocampal networks in both physiological and neurological disease states. An example of a topic that may be investigated with the described technique is the characterisation of the aberrant functional connectivity between the hippocampus and entorhinal cortex that may underlie epileptogenesis in TLE. For such studies, experimental models that provide more accurate representations of the pathophysiology of specific human epilepsies should be utilised. The results from this study also showcase the therapeutic potential of EIT for improving surgical outcome in patients with refractory epilepsy by improving the localisation of epileptogenic tissue for surgical resection and thus support the translatability of this technique to the clinical setting.

Author contribution statement

Sana Hannan: Conceptualisation, Data curation, Formal analysis, Investigation, Methodology, Visualisation, Writing – original draft preparation, Writing – reviewing and editing; Mayo Faulkner: Investigation, Methodology, Resources, Software; Kirill Aristovich: Formal analysis, Resources, Software; James Avery: Methodology, Software; Matthew C. Walker: Methodology; David S. Holder: Conceptualisation, Funding acquisition, Supervision, Writing – reviewing and editing.

Acknowledgments

This work was supported by grants from DARPA (N66001-16-2-4066), Blackrock Microsystems and the EPSRC (EP/M506448/1). James Avery was supported by the NIHR Imperial BRC.

Appendix A. Supplementary data

Supplementary data to this article can be found online at https://doi.org/10.1016/j.neuroimage.2020.116525.

References

Ahlfors, S.P., Han, J., Lin, F., Witzel, T., Belliveau, J.W., Hämäläinen, M.S., Halgren, E., 2010. Cancellation of EEG and MEG signals generated by extended and distributed sources. Hum. Brain Mapp. 31 (1), 140–149.

Ahrens, M.B., Orger, M.B., Robson, D.N., Li, J.M., Keller, P.J., 2013. Whole-brain functional imaging at cellular resolution using light-sheet microscopy. Nat. Methods 10 (5), 413–420.

Andersen, P., Bliss, T.V., Skrede, K.K., 1971. Unit analysis of hippocampal population spikes. Exp. Brain Res. 13 (2), 208–221.

Aristovich, K.Y., Sato dos Santos, G., Packham, B.C., Holder, D.S., 2014. A method for reconstructing tomographic images of evoked neural activity with electrical impedance tomography using intracranial planar arrays. Physiol. Meas. 35, 1095–1109.

Aristovich, K.Y., Packham, B.C., Koo, H., dos Santos, G.S., McEvoy, A., Holder, D.S., 2016. Imaging fast electrical activity in the brain with electrical impedance tomography. Neuroimage 124 (Pt A), 204–213.

Aristovich, K., Donegá, M., Blochet, C., Avery, J., Hannan, S., Chew, D.J., Holder, D., 2018. Imaging fast neural traffic at fascicular level with electrical impedance tomography: proof of principle in rat sciatic nerve. J. Neural Eng. 15 (5), 056025.

Avery, J., Dowrick, T., Faulkner, M., Goren, N., Holder, D.S., 2017. A versatile and reproducible multi-frequency electrical impedance tomography system. Sensors 17 (2), E280.

Avery, J., Dowrick, T., Witkowska-Wrobel, A., Faulkner, M., Aristovich, K., Holder, D., 2019. Simultaneous EIT and EEG using frequency division multiplexing. Physiol. Meas. 40 (3), 034007.

Awad, I.A., Rosenfeld, J., Ahl, J., Hahn, J.F., Lüders, H., 1991. Intractable epilepsy and structural lesions of the brain: mapping, resection strategies, and seizure outcome. Epilepsia 32 (2), 179–186.

Baumann, S.B., Wozny, D.R., Kelly, S.K., Meno, F.M., 1997. The electrical conductivity of human cerebrospinal fluid at body temperature. IEEE Trans. Biomed. Eng. 44 (3), 220–223.

Berg, A.T., Berkovic, S.F., Brodie, M.J., Buchhalter, J., Cross, J.H., van Emde Boas, W., Scheffer, I.E., 2010. Revised terminology and concepts for organization of seizures and epilepsies: report of the ILAE Commission on Classification and Terminology, 2005-2009. Epilepsia 51 (4), 676–685.

Berkovic, S.F., Andermann, F., Olivier, A., Ethier, R., Melanson, D., Robitaille, Y., . . Feindel, W., 1991. Hippocampal sclerosis in temporal lobe epilepsy demonstrated by magnetic resonance imaging. Ann. Neurol. 29 (2), 175–182.

Blair, R.D., 2012. Temporal lobe epilepsy semiology. Epilepsy Res. Treat. 751510.

Boverman, G., Kim, B.S., Isaacson, D., Newell, J.C., 2007. The complete electrode model for imaging and electrode contact compensation in electrical impedance tomography. Conf. Proc. IEEE Eng. Med. Biol. Soc. 3462–3465.

Bragin, A., Penttonen, M., Buzsáki, G., 1997. Termination of epileptic afterdischarge in the hippocampus. J. Neurosci. 17 (7), 2567–2579.

Brown, B.H., 2003. Electrical impedance tomography (EIT): a review. J. Med. Eng. Technol. 27 (3), 97–108.

Burianová, H., Faizo, N.L., Gray, M., Hocking, J., Galloway, G., Reutens, D., 2017. Altered functional connectivity in mesial temporal lobe epilepsy. Epilepsy Res. 137, 45–52.

Colangeli, R., Pierucci, M., Benigno, A., Campiani, G., Butini, S., Di Giovanni, G., 2017. The FAAH inhibitor URB597 suppresses hippocampal maximal dentate afterdischarges and restores seizure-induced impairment of short and long-term synaptic plasticity. Sci. Rep. 7 (1), 11152.

Corley, J.A., Nazari, P., Rossi, V.J., Kim, N.C., Fogg, L.F., Hoeppner, T.J., Byrne, R.W., 2017. Cortical stimulation parameters for functional mapping. Seizure 45, 36–41.

Diehl, B., Lüders, H.O., 2000. Temporal lobe epilepsy: when are invasive recordings needed? Epilepsia 41 (3), S61–S74.

Dowrick, T., Sato dos Santos, G., Vongerichten, A., Holder, D., 2015. Parallel, multi frequency EIT measurement, suitable for recording impedance. J. Electr. Bioimpedance 6, 37–43.

Dümpelmann, M., Ball, T., Schulze-Bonhage, A., 2012. sLORETA allows reliable distributed source reconstruction based on subdural strip and grid recordings. Hum. Brain Mapp. 33 (5), 1172–1188.

Engel, J.J., 2001. Mesial temporal lobe epilepsy: what have we learned? The Neuroscientist 7 (4), 340–352.

Faulkner, M., Jehl, M., Aristovich, K., Avery, J., Witkowska-Wrobel, A., Holder, D., 2017. Optimisation of current injection protocol based on a region of interest. Physiol. Meas. 38 (6), 1158–1175.

Faulkner, M., Hannan, S., Aristovich, K., Avery, J., Holder, D., 2018a. Feasibility of imaging evoked activity throughout the rat brain using electrical impedance tomography. Neuroimage 178, 1–10.

Faulkner, M., Hannan, S., Aristovich, J., Avery, J., Holder, D., 2018b. Characterising the frequency response of impedance changes during. Physiol. Meas. 39 (3), 034007.

Hannan, S., 2019. Imaging Fast Neural Activity in the Brain during Epilepsy with Electrical Impedance Tomography. PhD thesis. University College, London, UK.

Hannan, S., Faulkner, M., Aristovich, K., Avery, J., Holder, D., 2018a. Imaging fast electrical activity in the brain during ictal epileptiform discharges with electrical impedance tomography. NeuroImage Clin. 20, 674–684.

Hannan, S., Faulkner, M., Aristovich, K., Avery, J., Holder, D., 2018b. Frequency-dependent characterisation of impedance changes during epileptiform activity in a rat model of epilepsy. Physiol. Meas. 39 (8), 095003.

Hannan, S., Faulkner, M., Aristovich, K., Avery, J., Holder, D., 2019. Investigating the safety of fast neural electrical impedance tomography in the rat brain. Physiol. Meas. 40 (3), 034003.

Heeger, D.J., Ress, D., 2002. What does fMRI tell us about neuronal activity? Nat. Rev. Neurosci. 3 (2), 142–151.

Hennessy, M.J., Elwes, R.D., Binnie, C.D., Polkey, C.E., 2000. Failed surgery for epilepsy. A study of persistence and recurrence of seizures following temporal resection. Brain 123 (Pt 12), 2445–2466.

Hillman, E.M., 2007. Optical brain imaging in vivo: techniques and applications from animal to man. J. Biomed. Opt. 12 (5), 051402.

Holder, D.S., 2005. Electrical Impedance Tomography: Methods, History and Applications. Institute of Physics Publishing, Bristol.

Horesh, L., 2006. Some Novel Approaches in Modelling and Image Reconstruction for Multi Frequency Electrical Impedance Tomography of the Human Brain. PhD thesis. University College, London, UK.

Hunold, A., Funke, M.E., Eichardt, R., Stenroos, M., Haueisen, J., 2016. EEG and MEG: sensitivity to epileptic spike activity as function of source orientation and depth. Physiol. Meas. 37 (7), 1146–1162.

Janz, P., Savanthrapadian, S., Häussler, U., Kilias, A., Nestel, S., Kretz, O., Haas, C.A., 2017. Synaptic remodeling of entorhinal input contributes to an aberrant hippocampal network in temporal lobe epilepsy. Cerebr. Cortex 27 (3), 2348–2364.

Jatoi, M.A., Kamel, N., Malik, A.S., Faye, I., Begum, T., 2014. A survey of methods used for source localization using EEG signals. Biomed. Signal Process. Control 11, 42–52.

Javidan, M., 2012. Electroencephalography in mesial temporal lobe epilepsy: a review. Epilepsy Res. Treat. 637430.

Jehl, M., Dedner, A., Betcke, T., Aristovich, K., Klöfkorn, R., Holder, D., 2015. A fast parallel solver for the forward problem in electrical impedance tomography. IEEE Trans. Biomed. Eng. 62 (1), 126–137.

Jehl, M., Aristovich, K., Faulkner, M., Holder, D., 2016. Are patient specific meshes required for EIT head imaging? Physiol. Meas. 37, 879–892.

Kajikawa, Y., Schroeder, C.E., 2011. How local is the local field potential? Neuron 72 (5), 847–858.

Kandratavicius, L., Balista, P.A., Lopes-Aguiar, C., Ruggiero, R.N., Umeoka, E.H., Garcia-Cairasco, N., Leite, J.P., 2014. Animal models of epilepsy: use and limitations. Neuropsychiatric Dis. Treat. 10, 1693–1705.

Klivington, K.A., Galambos, R., 1967. Resistance shifts accompanying the evoked cortical response in the cat. Science 157 (3785), 211–213.

Kondo, M., Kobayashi, K., Ohkura, M., Nakai, J., Matsuzaki, M., 2017. Two-photon calcium imaging of the medial prefrontal cortex and hippocampus without cortical invasion. Elife 6, e26839.

Kwan, P., Schachter, S.C., Brodie, M.J., 2011. Drug-resistant epilepsy. N. Engl. J. Med. 365 (10), 919–926.

Latikka, J., Kuurne, T., Eskola, H., 2001. Conductivity of living intracranial tissues. Phys. Med. Biol. 46 (6), 1611–1616.

Lesser, R.P., Lüders, H., Klem, G., Dinner, D.S., Morris, H.H., Hahn, J.F., Wyllie, E., 1987. Extraoperative cortical functional localization in patients with epilepsy. J. Clin. Neurophysiol. 4 (1), 27–53.

Lesser, R.P., Crone, N.E., Webber, W.R., 2010. Subdural electrodes. Clin. Neurophysiol. 121 (9), 1376–1392.

Lionheart, W.R., 2004. EIT reconstruction algorithms: pitfalls, challenges and recent developments. Physiol. Meas. 25 (1), 125–142.

Logothetis, N.K., Pauls, J., Augath, M., Trinath, T., Oeltermann, A., 2001. Neurophysiological investigation of the basis of the fMRI signal. Nature 412 (6843), 150–157.

Lüders, H., 2008. Textbook of Epilepsy Surgery. Informa Healthcare, London.

Ma, H., Zhao, M., Schwartz, T.H., 2013. Dynamic neurovascular coupling and uncoupling during ictal onset, propagation, and termination revealed by simultaneous in vivo optical imaging of neural activity and local blood volume. Cerebr. Cortex 23 (4), 885–899.

Nair, D.R., 2016. Management of drug-resistant epilepsy. Continuum 22 (1), 157–172.

Nie, B., Chen, K., Zhao, S., Liu, J., Gu, X., Yao, Q., Shan, B., 2013. A rat brain MRI template with digital stereotaxic atlas of fine anatomical delineations in paxinos space and its automated application in voxel-wise analysis. Hum. Brain Mapp. 34 (6), 1306–1318.

Oh, T., Gilad, O., Ghosh, A., Schuettler, M., Holder, D.S., 2011. A novel method for recording neuronal depolarization with recording at 125-825 Hz: implications for imaging fast neural activity in the brain with electrical impedance tomography. Med. Biol. Eng. Comput. 49 (5), 593–604.

Olsson, T., Broberg, M., Pope, K.J., Wallace, A., Mackenzie, L., Blomstrand, F., Willoughby, J.O., 2006. Cell swelling, seizures and spreading depression: an impedance study. Neuroscience 140 (2), 501–515.

Packham, B.C., 2013. Imaging Fast Neural Activity in the Brain with Electrical Impedance Tomography. PhD thesis. University College, London, UK.

Pan, E., Stringer, J.L., 1997. Role of potassium and calcium in the generation of cellular bursts in the dentate gyrus. J. Neurophysiol. 77 (5), 2293–2299.

Paxinos, G., Watson, C., 2013. The Rat Brain in Stereotaxic Coordinates, seventh ed. Academic Press, San Diego.
Pillay, P.K., Barnett, G., Awad, I., 1992. MRI-guided stereotactic placement of depth electrodes in temporal lobe epilepsy. Br. J. Neurosurg. 6 (1), 47–53.
Pouratian, N., Cannestra, A.F., Bookheimer, S.Y., Martin, N.A., Toga, A.W., 2004. Variability of intraoperative electrocortical stimulation mapping parameters across and within individuals. J. Neurosurg. 101 (3), 458–466.
Quiroga, R.Q., Nadasdy, Z., Ben-Shaul, Y., 2004. Unsupervised spike detection and sorting with wavelets and superparamagnetic clustering. Neural Comput. 16 (8), 1661–1687.
Ranck, J.B., 1963. Specific impedance of rabbit cerebral cortex. Exp. Neurol. 7, 144–152.
Renvall, V., Nangini, C., Hari, R., 2014. All that glitters is not BOLD: inconsistencies in functional MRI. Sci. Rep. 4 (3920).
Scharfman, H.E., 1994. EPSPs of dentate gyrus granule cells during epileptiform bursts of dentate hilar "mossy" cells and area CA3 pyramidal cells in disinhibited rat hippocampal slices. J. Neurosci. 14 (10), 6041–6057.
Scharfman, H.E., 1996. Conditions required for polysynaptic excitation of dentate granule cells by area CA3 pyramidal cells in rat hippocampal slices. Neuroscience 72 (3), 655–668.
Schomer, D.L., Lopes da Silva, F.H., 2010. Niedermeyer's Electroencephalography : Basic Principles, Clinical Applications, and Related Fields, sixth ed. Lippincott Williams & Wilkins, Philadelphia; London.
Shepherd, G.M., 2004. The Synaptic Organisation of the Brain, fifth ed. Oxford University Press, New York.
So, E.L., Alwaki, A., 2018. A guide for cortical electrical stimulation mapping. J. Clin. Neurophysiol. 35 (2), 98–105.
Somersalo, E., Cheney, M., Isaacson, D., 1992. Existence and uniqueness for electrode models for electric current computed tomography. SIAM J. Appl. Math. 52, 1023–1040.
Spencer, S.S., 1981. Depth electroencephalography in selection of refractory epilepsy for surgery. Ann. Neurol. 9 (3), 207–214.
Spencer, S.S., 1996. Long-term outcome after epilepsy surgery. Epilepsia 37 (9), 807–813.
Spencer, S.S., Berg, A.T., Vickrey, B.G., Sperling, M.R., Bazil, C.W., Shinnar, S., Frobish, D., 2003. Initial outcomes in the multicenter study of epilepsy surgery. Neurology 61 (12), 1680–1685.
Stosiek, C., Garaschuk, O., Holthoff, K., Konnerth, A., 2003. In vivo two-photon calcium imaging of neuronal networks. Proc. Natl. Acad. Sci. U. S. A. 100 (12), 7319–7324.
Theodore, W.H., Bhatia, S., Hatta, J., Fazilat, S., DeCarli, C., Bookheimer, S.Y., Gaillard, W.D., 1999. Hippocampal atrophy, epilepsy duration, and febrile seizures in patients with partial seizures. Neurology 52 (1), 132–136.
Tikhonov, A.N., Goncharsky, A., Stepanov, V., Yagola, A., 1995. Numerical Methods for the Solution of Ill-Posed Problems. Kluwer Academic Publishers, Dordrecht, The Netherlands.
Tsurugizawa, T., Ciobanu, L., Le Bihan, D., 2013. Water diffusion in brain cortex closely tracks underlying neuronal activity. Proc. Natl. Acad. Sci. U. S. A. 110 (28), 11636–11641.
Ullah, G., Wei, Y., Dahlem, M.A., Wechselberger, M., Schiff, S.J., 2015. The role of cell volume in the dynamics of seizure, spreading depression, and anoxic depolarization. PLoS Comput. Biol. 11 (8), e1004414.
Vongerichten, A.N., Sato Dos Santos, G.S., Aristovich, K., Avery, J., McEvoy, A., Walker, M., Holder, D.S., 2016. Characterisation and imaging of cortical impedance changes during interictal and ictal activity in the anaesthetised rat. Neuroimage 124 (Pt A), 813–823.
Voorhies, J.M., Cohen-Gadol, A., 2013. Techniques for placement of grid and strip electrodes for intracranial epilepsy surgery monitoring: pearls and pitfalls. Surg. Neurol. Int. 4, 98.
Walker, M.C., 2015. Hippocampal sclerosis: causes and prevention. Semin. Neurol. 35 (3), 193–200.
Walker, M.C., Perry, H., Scaravilli, F., Patsalos, P.N., Shorvon, P.N., Jefferys, J.G., 1999. Halothane as a neuroprotectant during constant stimulation of the perforant path. Epilepsia 40 (3), 359–364.
Witkowska-Wrobel, A., Aristovich, K., Faulkner, M., Avery, J., Holder, D., 2018. Feasibility of imaging epileptic seizure onset with EIT and depth electrodes. Neuroimage 173, 311–321.
Wyler, A.R., 1992. Subdural strip electrodes in surgery of epilepsy. In: Lüders, H. (Ed.), Epilepsy Surgery. Raven Press, New York, pp. 395–398.